ADVANCED OPTICAL MATERIALS
www.advopticalmat.de

Bay-functionalized [7]Helicene Bilayer Nanographenes

*Anmol Thanai, Vikas Sharma, Louis Minion, Hassan Khan, Hadeel Abbas, George F. S. Whitehead, Avantika Hasija, Jessica Wade, Matthew John Fuchter, and Ashok Keerthi**

Helical bilayer nanographenes (HBNGs) represent a promising class of materials for advanced optoelectronic and chiroptical applications, owing to their extended π-conjugation, intrinsic chirality, and tunable interlayer interactions. Here, the rational design and synthesis of *bay*-functionalized [7]HBNGs incorporating methoxy, diketone, and phenazine moieties is reported. These tailored modifications enable precise tuning of redox properties and significantly enhance photophysical properties, including pronounced spectral shifts, prolonged fluorescence lifetimes of up to 10 ns, and fluorescence quantum yields reaching 55%. Importantly, the resulting [7]HBNGs exhibit strong electronic circular dichroism and exceptional circularly polarized luminescence (CPL), with CPL brightness values as high as 110 M^{-1} cm^{-1}. The modular, convergent strategy enables versatile late-stage modification of bay-substituted HBNGs from a single scalable precursor, streamlining access to diverse derivatives and opening new opportunities for their application in molecular electronics, chiroptical devices, and advanced optoelectronic materials.

1. Introduction

Nanographenes, atomically precise fragments of graphene, have attracted significant attention due to their exceptional electronic and optical properties, which stem from quantum confinement effects.[1–3] Prolonged efforts to functionalize nanographenes have resulted in the production of α-diketones,[4] quinoxalines,[5] and N-heterosuperbenzenes,[6] which are building blocks for 3D structures with applications in organic semiconductors.[7] Along with that, the introduction of helicity[8,9] into nanographenes[10,11] has enabled enabled a new class of chiral architectures, including bilayer helical nanographenes[12] with broad potential across applications ranging from optoelectronics,[13] photonics,[14,15] spintronics[16] to circularly polarized luminescence (CPL).[17–21] Their tunable interlayer π–π interactions significantly influence electronic coupling and chiroptical behavior,[22–27] offering unique opportunities for advanced material design.

Recent progress has significantly deepened our understanding of the structure-chiroptical property relationships in helical bilayer nanographenes (HBNGs). Key advances include elucidating how helicene length influences chiroptical behavior,[22,27] controlling molecular orientation to tune charge-transfer characteristics,[28] achieving chiroptical amplification through appended chiral moieties,[23,29] and revealing the effects of regioisomeric π-extension on phosphorescence.[30]

A. Thanai, V. Sharma, H. Khan, H. Abbas, G. F. S. Whitehead, A. Hasija, A. Keerthi
Department of Chemistry
School of Natural Sciences
The University of Manchester
Oxford Road, Manchester M13 9PL, UK
E-mail: ashok.keerthi@manchester.ac.uk

L. Minion, J. Wade
Department of Materials
Imperial College London
Prince Consort Road, London SW7 2AZ, UK

L. Minion, J. Wade, M. J. Fuchter
Centre for Processable Electronics
Imperial College London
London SW7 2AZ, UK

The ORCID identification number(s) for the author(s) of this article can be found under https://doi.org/10.1002/adom.202502564

DOI: 10.1002/adom.202502564

L. Minion, J. Wade
Diamond Light Source Ltd.
Harwell Science and Innovation Campus
Didcot, Oxfordshire OX11 0DE, UK

M. J. Fuchter
Department of Chemistry
Molecular Science Research Hub
Imperial College London
London W12 0BZ, UK

M. J. Fuchter
Department of Chemistry
Chemistry Research Laboratory
University of Oxford
12 Mansfield Road, Oxford OX1 3TA, UK

A. Keerthi
Photon Science Institute
The University of Manchester
Manchester M13 9PL, UK

A. Keerthi
National Graphene Institute
The University of Manchester
Booth St East, Manchester M13 9SS, UK

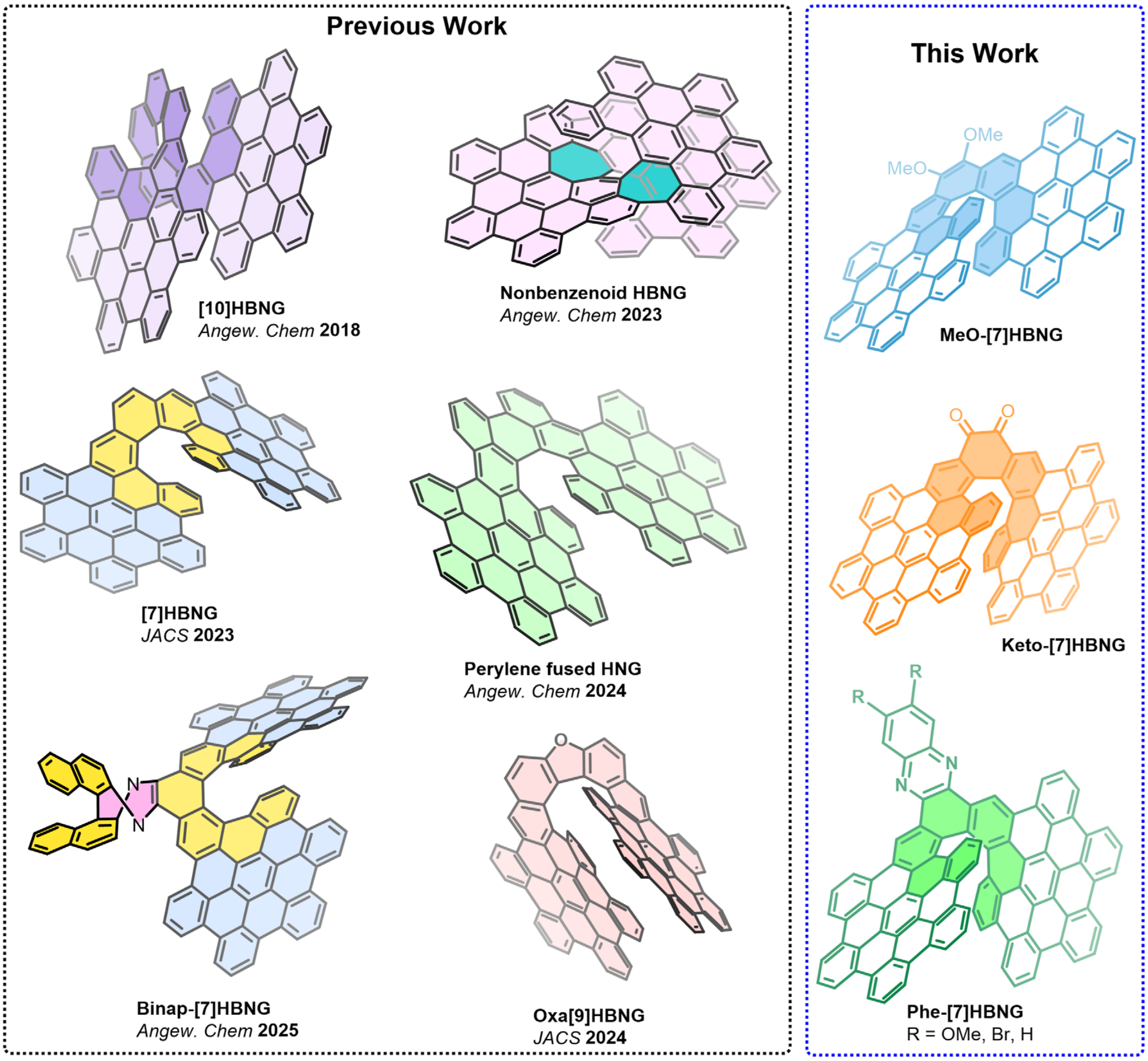

Figure 1. Chemical structures of representative examples of helical bilayer nanographenes (HBNGs), helical nanographenes (HNGs), and, from this work, *bay*-functionalized [7]HBNGs.

Additionally, important developments have emerged from exploring heteroatom doping,[30–33] multi-layered architectures,[34,35] and non-benzenoid scaffolds,[32,36] all contributing to the fine-tuning of the optical and electronic properties in this unique class of chiral π-extended materials.[11] Recent reports by Martín et al. has demonstrated catalytic enantioselective methods for synthesizing helicene-based nanographenes with outstanding enantiopurity and enhanced circularly polarized luminescence (CPL) performance, marking a key step forward in creating scalable chiral optoelectronic materials[37,38] Despite these advances, systematic investigations into how π-extension from the backbone of HBNGs affects their chiroptical properties remain limited, largely due to the complexity of precursors and the narrow scope of applicable reactions. Consequently, challenges persist in developing bilayer nanographene systems with diverse functionalities. Therefore, a synthetic approach that enables efficient construction of a wide variety of backbone π-extended HBNGs from readily accessible building blocks is highly desirable.

Herein, we report the synthesis of [7]helicene bilayer nanographenes ([7]HBNGs) functionalized with dimethoxy (**1**), diketone (**2**), methoxyphenazine (**3**), dibromophenazine (**4**), and phenazine (**5**) (**Figure 1** and **Scheme 1**) functional moieties. All these [7]HBNGs were derived from a methoxyphenanthrene precursor, namely 9,10-dimethoxy-3,6-bis(4',5',6'-triphenyl-[1,1':2',1''-terphenyl]-3'-yl)phenanthrene (**S3**), in a single or two-step reaction. The use of **S3** enables *bay*-functionalization of [7]HBNGs through a bottom-up synthesis approach and provides diverse functionality to the target helical structures. This modular, convergent route facilitates late-stage functional tuning of *bay*-substituted HBNGs from a single scalable scaffold, in contrast to the multiple separate synthetic campaigns required in earlier reports. For example, methoxy groups enhance solubility and electron-donating character, diketone units serve as reactive handles[39,40] for further modification,[40] and phenazine groups introduce redox-active centers[41,42] as well as further π-extension through *bay*-position. These tailored functional groups, when incorporated into bilayer architectures, enable precise tuning

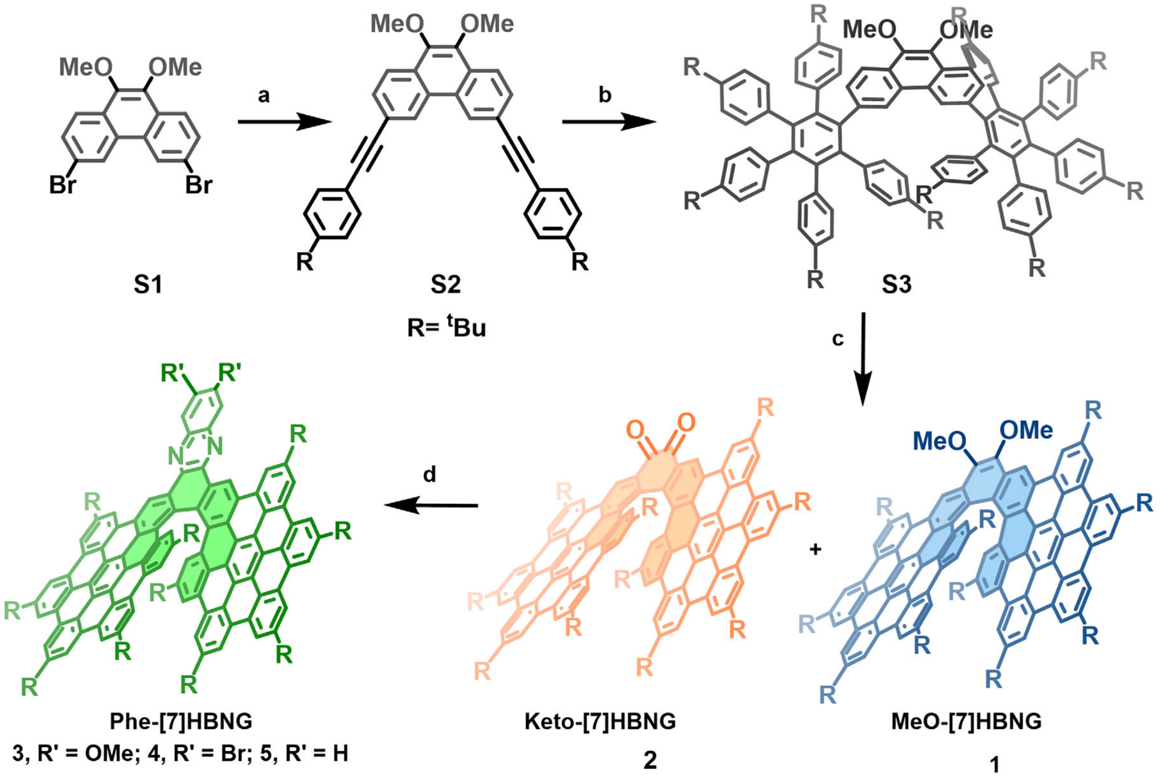

Scheme 1. Synthesis scheme of functionalized helical bilayer nanographenes (**1–5**); (a) 1-(tert-butyl)-4-ethynylbenzene, Et$_3$N:Toluene(1:5), Pd(PPh$_3$)$_4$, PPh$_3$, CuI, 80 °C, 15 h, yield 85%; (b) 2,3,4,5-tetrakis(4-(*tert*-butyl)phenyl)cyclopenta-2,4-diene-1-one, diphenyl ether, Microwave reactor 150 W, 260 °C, 90 min, yield 60%; (c) DDQ, DCM, TfOH, −10 °C, 90 min, yield 31% for 1 and 35% for **2** respectively; (d) AcOH, 4,5-dimethoxybenzene-1,2-diamine, 100 °C, 12 h, yield 65% for **3**, AcOH, 4,5-dibromobenzene-1,2-diamine, 100 °C, 12 h, yield 71% for **4,** AcOH, benzene-1,2-diamine, 100 °C, 12 h, yield 88% for **5**. R: *tert*-butyl; DDQ: 2,3-dichloro-5,6- dicyano-1,4-benzoquinone; TfOH: trifluoromethanesulfonic acid; DCM: dichloromethane; AcOH: acetic acid.

of optical properties as confirmed by a significant shift in fluorescence spectra and up to 55% fluorescence quantum yield. Through synthetic methodologies, crystallographic studies, spectroscopic characterization, and computational modelling, this work establishes these [7]HBNGs as advanced CPL-active materials for prospective chiroptical applications.

2. Results and Discussion

Compound **2**, a diketone-functionalized nanographene, was synthesized through a three-step procedure (**Scheme 1**). First, Sonogashira coupling reaction between 3,6-dibromo-9,10-dimethoxyphenanthrene (**S1**) and 1-(*tert*-butyl)-4-ethynylbenzene yielded compound **S2**, 3,6-bis((4-(*tert*-butyl) phenyl) ethynyl)-9,10-dimethoxyphenanthrene in 85% yield. In the second step, a two-fold Diels–Alder reaction on **S2** with 2,3,4,5-tetrakis(4-(*tert*-butyl) phenyl) cyclopenta-2,4-dien-1-one produced the methoxy-substituted phenylene precursor (**S3**) in 60% yield after column chromatography purification on silica gel.

Subsequently, a Scholl-type cyclodehydrogenation reaction was carried out using DDQ as the oxidant, triflic acid (TfOH) as the Brønsted acid, and dry DCM as the reaction solvent. The reaction was conducted at −10 °C for 60 min to afford a mixture of compound (**1**) and compound (**2**) in 31% and 35% yield, respectively. Extending the reaction time to 100 min and allowing the temperature to reach 0 °C resulted in an increased yield of compound **2** (60%), while the yield of compound **1** significantly decreased (≈5%). These observations suggest that under DDQ/acidic conditions, in situ demethylation of the methoxy groups in **1** occurred, followed by further oxidation to yield compound **2**. Notably, the resulting diketo derivatives can theoretically be reverted to their methoxy precursors by reductive methylation, as demonstrated previously on related polycyclic aromatic hydrocarbons, although this transformation was not performed on the compounds reported herein.[43] Finally, compound **2** was reacted with 4,5-dimethoxybenzene-1,2-diamine, 4,5-dibromobenzene-1,2-diamine, and benzene-1,2-diamine in the presence of acetic acid to afford compound **3** (yield 65%), compound **4** (yield 71%), and compound **5** (yield 88%), respectively, in moderate to high yields.

Hence, acid-promoted condensation of helicene diketone with various aromatic diamines proceeds efficiently under mild conditions, enabling modular access to phenazine-fused helicenes with diverse substituents. This cyclocondensation strategy may be conceptually extended to the construction of macrocyclic architectures, potentially enabling donor-acceptor systems, nanohoops, nanohoop dimers, and nanobelts, though specific applications would require further investigation.[44] Particularly, recent reports have demonstrated a broad substrate scope, with yields ranging from moderate to high using sterically hindered,

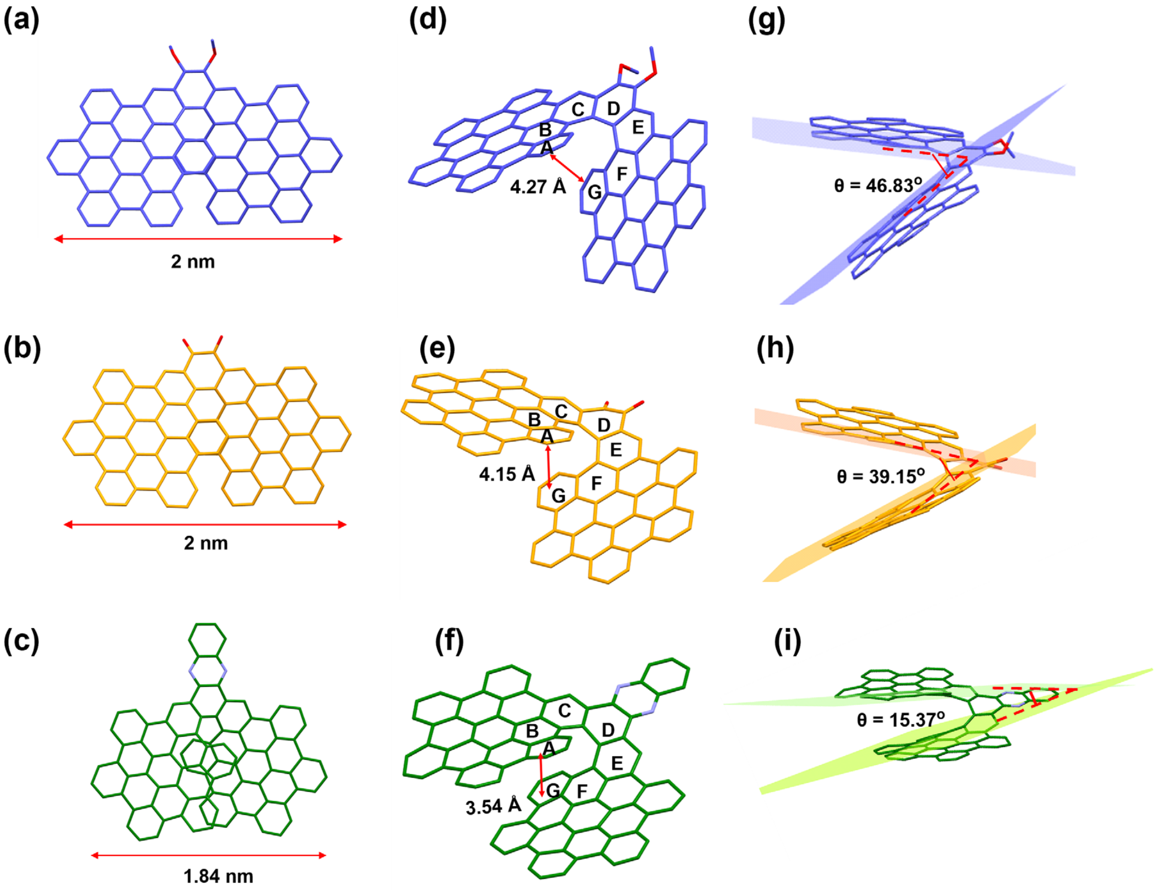

Figure 2. Single-crystal analysis of helical bilayer nanographene molecules **1**, **2,** and **5**. (a–c) Top view of the crystal structures compound (**1**) and compound (**2**) and compound (**5**); (d–f) Side view of the crystal structures showing distance of centroid of rings A and G (helical pitch, d_{AG}) and inner torsional angles between rings A to G; (g–i) Dihedral angle between the two planes (θ_{AG}) of the terminal rings A and G; Solvent molecules, *tert*-butyl groups and hydrogen atoms on the single crystal structures are omitted for clarity.

electron-rich, and electron-deficient diamines under standard acidic conditions.[39,45]

Beyond condensation chemistry, helicene diketones have also been shown to undergo [4+2] photocycloaddition reactions with dienophiles such as 2,3-dimethylbut-2-ene, furnishing dioxane-fused helical nanographenes.[46] This alternative approach offers a complementary route to incorporate dioxane functionality on the *bay*-position of the helical nanographene system. Additionally, the dibromo functionality of **4** serves as a multipurpose synthetic handle for π-extension through C-C coupling reactions,[47] facilitating access to diverse supramolecular systems as well as N-rich helical molecules that are currently under active investigation in our research group.

Synthesized compounds were unambiguously characterized using ^{1}H, ^{13}C nuclear magnetic resonance (NMR) spectroscopy, high-resolution mass spectrometry analysis, and matrix-assisted laser desorption/ionization mass spectrometry (MALDI-TOF MS), as well as other spectroscopic characterization (see supporting information). Chemical structures of compounds **1**, **2**, and **5** were conclusively validated by single-crystal X-ray diffraction (SC-XRD) analysis (**Figure 2**). Racemic crystals of **1** were obtained by slow evaporation of a chlorobenzene solution at room temperature, crystals of **2** were successfully grown from a 1:1 hexane–dichloromethane mixture, while a chloroform-methanol mixture was employed for crystallizing compound **5**. In contrast, crystals of compound **3** exhibited poor diffraction quality and could not be resolved.

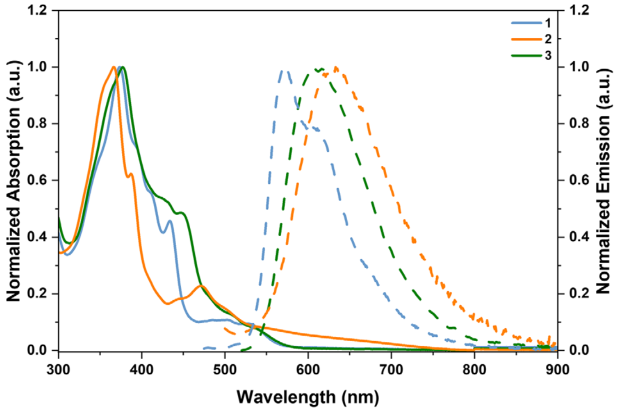

Figure 3. Normalized UV–vis absorption spectra (solid curves) and fluorescence spectra (dotted curves) of **1**–**3** in chloroform solutions (≈10^{-5} M) at room temperature.

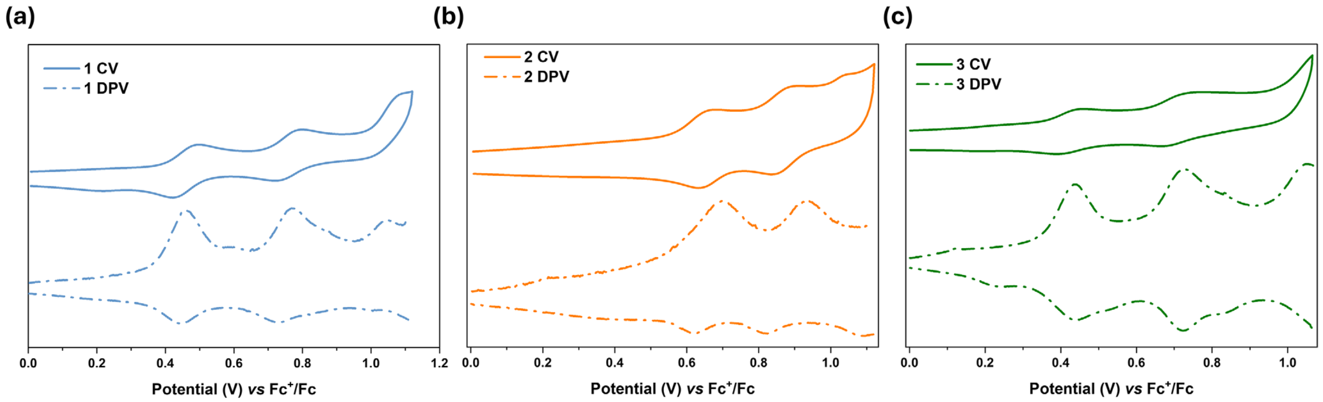

Figure 4. Cyclic voltammetry (solid curves) and differential pulse voltammetry (dotted curves) of **1**, **2,** and **3** in DCM (vs Fc+ /Fc, Fc = ferrocene), containing 0.1 M AND of tetrabutylammonium hexafluorophosphate (nBu_4NPF_6) at a scan rate of 100 mVs^{-1} at room temperature. (Glassy carbon, silver wire, and Pt wire were used as the working electrode, the pseudo-reference electrode, and the counter electrode, respectively).

Compound **1** crystallized in a centrosymmetric monoclinic space group $P2_1/n$, whereas compound **2** crystallized similarly to compound **5** in the centrosymmetric triclinic space group *P-1*. The SC-XRD analysis revealed helical layered structures for **1** (Figure 2a,d,g), **2** (Figure 2b,e,h), and **5** (Figure 2c,f,i), with both enantiomers (***P***/***M***) present in a 1:1 ratio within the crystal packing (Figures S5,S8, and S11, Supporting Information). Interestingly, two distinct packing arrangements were observed for compound **1** within the unit cell (Figure S4, Supporting Information), attributed to the presence of rotational isomers of (***P***)-**1** and (***M***)-**1** enantiomers. This was further supported by intermolecular π–π stacking interactions between the ***P***- and ***M***-enantiomers and their respective rotational isomers, giving rise to an alternating AB-type packing pattern. Notably, the interlayer distance between the two rotational isomers remained consistent at 3.56 Å (Figure S5, Supporting Information). In contrast, compounds **2** and **5** displayed an AA-type packing motif.

In compound **1**, the two HBC layers linked by a [7] helicene unit display an interlayer distance of 4.27 Å, measured between the centroids of the terminal A and G rings (Figure 2d). Compound **2** shows a slightly shorter distance of 4.15 Å (Figure 2e), while compound **5** has the shortest interlayer separation at 3.54 Å (Figure 2f). These changes in interlayer distance correlate with the interplanar dihedral angle (θ_{AG}) between the two HBC layers, calculated from the planes defined by the A and G rings, which decrease progressively from 46.83° (**1**) to 39.15° (**2**) and 15.37° (**5**) (Figure 2g–i). This decreasing θ_{AG} is a cumulative effect of increasing molecular planarity due to the substituent effect and attractive dispersion forces due to π-extension in the helical framework, as previously also reported by Yusuke et al.[48] The phenazine backbone further extends the π-conjugation, and its flat geometry reduces the interhelical twist. This enforces a more planar structure, which stabilizes face-to-face π–π interactions and leads to the observed shorter interlayer distance. Thus, the incorporation of phenazine directly controls the solid-state packing, leading to stronger interhelical interactions.

During our study on phenazine derivatives, compound **5** was reported by Dongre et al.[23] using a slightly different synthesis approach, where they conducted cyclodehydrogenation of polyphenylene precursor after phenazine formation. Surprisingly, SC-XRD analysis of our compound **5** displayed a significant difference in unit cell parameters, helical pitch, and dihedral angles in comparison to the reported structure. Specifically, the interplanar angle (θ_{AG}) in our structure is 15.37°, compared to 18.09° in the reported structure,[23] while the terminal ring separation (helical pitch, d_{AG}) is reduced to 3.54 Å from 3.62 Å (Figure 2i). While comparing, our crystal of **5** exhibited the same centrosymmetric triclinic space group *P-1* as reported crystals[23] but different unit cell parameters, revealing polymorphism with altered twist angles.

The observed polymorphism between our structure and the previously reported one likely originates from the different crystallization solvents employed. While Dongre et al.[23] used a dichloromethane/n-hexane (1:2) mixture, we obtained single crystals from a chloroform/methanol (1:1) system. This solvent change facilitated the formation of a polymorph with a reduced interplanar dihedral angle (θ_{AG}) and shorter π-stacking distance, underscoring the significant influence of crystallization conditions on the final solid-state structure. This reduction in the θ_{AG} directly influences the molecular geometry and is expected to correspondingly alter the angle between the electric (μ_e) and magnetic (μ_m) transition dipole moments, which governs chiroptical activity and radiative decay pathways in the solid state.

The optical properties of helical bilayer nanographenes **1** to **3** were systematically examined using UV–vis absorption and fluorescence spectroscopy in anhydrous chloroform solutions (**Figure 3**). The absorption spectrum of **1** exhibited a broad, unstructured band in the UV region λ_{max} at 374 nm, along with extended shoulder bands in the visible region at 434 and 529 nm, with an absorption onset wavelength around 580 nm. In the case of compound **2**, broad absorption up to 800 nm was recorded in contrast to the ≈620 nm onset observed for the 7-diketo helicene.[49] This notable 180 nm red shift is attributed to the extended π-conjugation introduced by the bilayer nanographene framework. The broad peak from 500 to 800 nm is assigned to HOMO→LUMO transition (f = 0.59053) as well as attributed to charge transfer transition (Table S6, Supporting Information). The introduction of a dimethoxy phenazine moiety in compound **3** led to a pronounced absorption peak intensity (λ_{max} = 375 nm) extended into the visible region, with an onset wavelength around 600 nm. According to TD-DFT calculations, the $S_n \rightarrow S_1$ excitations for compounds **1** to **3** occur at 450, 451, and

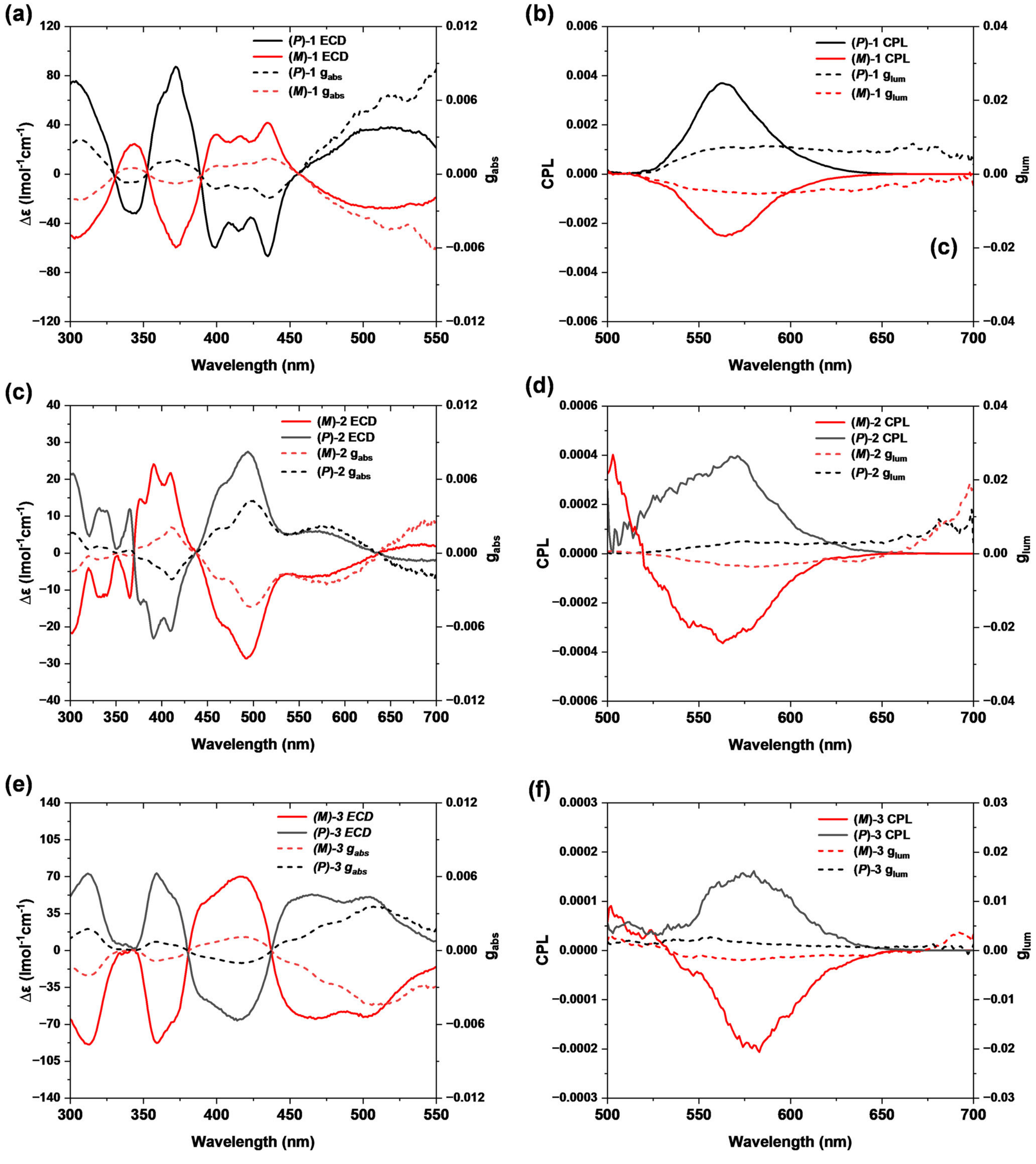

Figure 5. Electronic circular dichroism spectra of (***P***)-**1** and (***M***)-**1** (a); (***P***)-**2** and (***M***)-**2** (c), and (***P***)-**3** and (***M***)-**3** (e). Circularly polarized luminescence spectra of (***P***)-**1** and (***M***)-**1** (b); (***P***)-**2** and (***M***)-**2** (d), and (***P***)-**3** and (***M***)-**3** (f).

498 nm, respectively (Tables S6–S8 and Figure S27, Supporting Information).

Compound **2** exhibited weak fluorescence, with an emission maximum (λ_{em}) at 633 nm. This is in contrast to compounds **1** and **3**, which showed more intense emission peaks with λ_{em} at 572 nm and 606 nm, respectively. Notably, compounds **1** and **3** exhibited a shoulder peak around 617 nm. These values are red-shifted when compared to non-functionalized 7-helical bilayer nanographene (Table S4, Supporting Information, Entry 2) reported by Feng et al.,[34] Moreover, the emission bands of

Table 1. Comparison of optical and chiroptical parameters of compound **1–3**, (***P***)-**1**, c= 0.48×10^{-5} M, b) (***P***)-**2**, c= 1.95×10^{-5} M, (c) (***P***)-**3**, c= 0.67×10^{-5} M, respectively, in chloroform.

					S_1–S_0 transition[a)]			
HBNG	Φ	g_{abs} [10^{-3}]	g_{lum} [10^{-3}]	B_{CPL} [$M^{-1}.cm^{-1}$]	$\lvert\mu_e\rvert$ 10^{-18} (esu.cm)	$\lvert\mu_m\rvert$ 10^{-20} [erg.G^{-1}]	θ [deg]	$\lvert g_{lum}\rvert_{cal.}$ [10^{-3}]
(*P*)-1	0.40	6.4	7.1	110	4.74	3.44	75.45°	7.3
(*P*)-2	0.02	4.2	2.5	1.0	4.35	0.98	93.80°	0.5
(*P*)-3	0.55	3.5	1.4	31.9	3.65	2.51	85.36°	3.5

[a)] Calculated by TD-DFT at the CAM-b3lyp/def2TZVP level of theory.

functionalized HBNGs are considerably broader. This bathochromic shift and spectral broadening reflect the extended π-conjugation and altered electronic environments introduced by the substituents, which effectively narrow the HOMO–LUMO gap and modulate the emission properties. When comparing the emission bands for Phena-series, **4** displayed the most red-shifted band when compared to **3** and **5** (Figure S15, Supporting Information). Fluorescence lifetime decay measurements were carried out at room temperature, examined in anhydrous DCM solutions with pulsed 401 nm laser light (Figure S16 and Table S2, Supporting Information) to provide insights into the excited-state dynamics. The average fluorescence lifetimes for the racemic mixtures of helical nanographenes were determined to be 8.2 ns for **1**, 4.9 ns for **2**, and 10 ns for **3**. Fluorescence quantum yield (Φ_f) measurements in anhydrous chloroform further highlighted the influence of functional groups, with values of 40.2% for **1**, 2.0% for **2**, and 55.0% for **3**. Among the series, **3** shows the highest quantum yield due to dominant radiative decay, making it the most efficient fluorophore. In contrast, **2** has a very low quantum yield because non-radiative decay dominates. The presence of electron-donating dimethoxy groups in **3** leads to a higher quantum yield and better fluorescence lifetimes compared to previously reported systems such as phenazine-[7]helicene and biphenyl-[7]helicene[23] (Table S4, Supporting Information, Entries 15 and 16).

The electrochemical properties of **1–3** were studied by cyclic voltammetry (CV) and differential pulse voltammetry (DPV) in anhydrous DCM. Compound **1** exhibited two reversible oxidation waves at 0.46 and 0.76 V, while **2** showed reversible oxidations at 0.69 and 0.92 V. Compound **3** displayed two quasi-reversible oxidation waves at 0.43 and 0.63 V (all potentials vs. Fc^+/Fc; **Figure 4**). These values are notably lower than those of hexa-tert-butyl hexabenzocoronene (HBC), which have oxidation waves at 1.06 and 1.34 V *vs* Fc+/Fc, indicating easier oxidation.[50] The first oxidation potential ($E_{ox}1$) follows the order: compound (**3**) (0.43 V) < compound (**1**) (0.46 V) < compound (**2**) (0.69 V). Interestingly, this trend differs slightly from expectations based on π-conjugation extension and electronic nature, as compound (**1**) was anticipated to have the lowest potential due to its electron-rich helical backbone. The variation suggests that greater π–π overlapping between layers lowers oxidation potentials, consistent with earlier reports.[22,37] Bilayer graphene exhibits unique electronic properties based on layer positions and shows mixed valence effects related to layer overlap. In our case, the rigid phenazine backbone likely reduces interhelical twist/pitch and increases π–π overlapping of the HBC layers, as seen in crystal structures of similar compounds like compound (**5**). This stabilizes the radical cation and dication species ($E_{ox}1$ and $E_{ox}2$), enhancing interactions between the graphitized layers. (Figures S17–S19, Supporting Information).

The chiral resolution of the racemic compounds, **1-3,** into their respective enantiomerically pure (***P***/***M***) isomers was achieved using Lux 5 µm i-Amylose-3, LC Column 250 × 21.2 mm, and an isocratic mobile phase of n-hexane/DCM mixture at room temperature. After resolution (Figures S20–S22, Supporting Information), the chiroptical properties were studied (**Figure 5**; Figure S23, Supporting Information). The electronic circular dichroism (ECD) response was measured, and both enantiomers of three nanographenes displayed mirror images with several opposite Cotton effects in the UV–vis region.

The ECD spectrum of (***M***)-**1** exhibits three major negative Cotton effect bands at 307, 372, and 518 nm, along with two positive bands at 340 and 435 nm. In contrast, (***M***)-**2** shows two dominant negative Cotton effects at 303 nm and 497 nm, and weaker positive bands at 409 and 675 nm. Similarly, (***P***)-**3** displays two major positive bands at 311 and 507 nm, with a negative Cotton effect at 419 nm. The absolute configurations were assigned by comparing the experimental ECD spectra to TD-DFT-calculated spectra (Figures S24–S26, Supporting Information). The maximum molar circular dichroism ($\Delta\varepsilon_{max}$) values were observed as 86 $M^{-1}cm^{-1}$ for **1** at 372 nm, 29 $M^{-1}cm^{-1}$ for **2** at 492 nm, and 87 $M^{-1}cm^{-1}$ for **3** at 359 nm. Additionally, the maximum absorption dissymmetry factors ($|g_{abs}|_{max}$) were observed at 518 nm (6.4×10^{-3}), 497 nm (4.2×10^{-3}), and 508 nm (3.5×10^{-3}) for (***P***)- **1**, **2**, and **3** (Figure 5, **Table 1**; Table S5, Supporting Information).

The CPL spectra of enantiomeric compounds **1–3** were also measured in chloroform, showing significant g_{lum} values (Figure 5, Table 1; Table S5, Supporting Information). We note that in compounds **2** and **3**, the absolute g_{lum} values were greater for the (***M***) enantiomers than for the (***P***) enantiomers, whereas in compound **1**, the (***P***) enantiomer exhibited higher values than the (***M***) enantiomer. This variation is likely due to differences in enantiomeric purity (Figures S20–S22, Supporting Information).

For practical applications of CPL, achieving a high g_{lum}, high Φ_f, and a large molar extinction coefficient (ε) is essential. To assess the overall performance of CPL-active materials, the CPL brightness (B_{CPL}), defined as $B_{CPL} = (\varepsilon \times \Phi_f \times g_{lum})/2$, has been proposed.[51] However, developing high-performance helical molecular chromophores with excellent B_{CPL} values remains challenging, as maximizing Φ_f and g_{lum} simultaneously is inherently difficult due to their theoretical trade-off.[52] Among the compounds **1–3**, the strong ε and high Φ_f obtained for

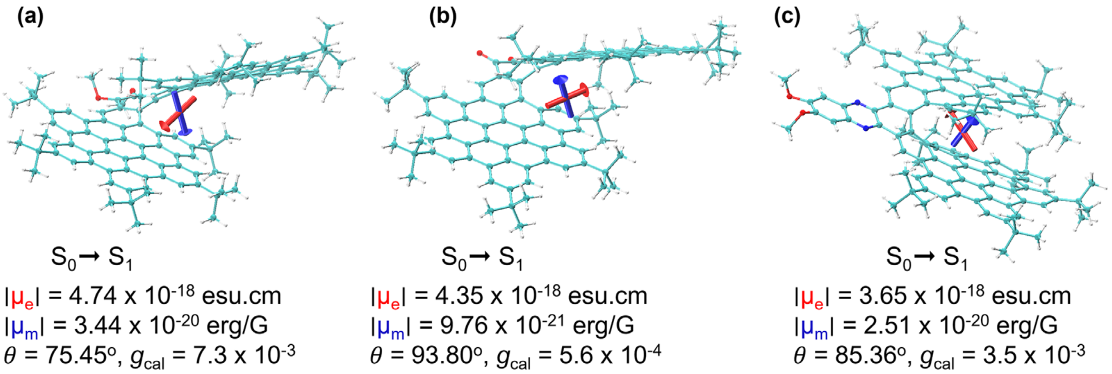

Figure 6. (a–c) Transition dipole moments for compounds **1-3** corresponding to the $S_n \rightarrow S_1$ electronic transition. Electric transition dipole moments (μ_e) are depicted in red, and magnetic transition dipole moments (μ_m) are shown in blue. The angle θ between the electric and magnetic dipole moment vectors determines the magnitude of the calculated dissymmetry factor according to the expression $g = 4 \cos \theta \times |\mu_m|/|\mu_e|$.

compounds **1** and **3** resulted in significant CPL brightness. Estimated B_{CPL} values were 110 M^{-1} cm^{-1} for (***P***)-**1**, 1.0 M^{-1} cm^{-1} for (***P***)-**2**, and 31.9 M^{-1} cm^{-1} for (***P***)-**3** (Table 1; Table S5, Supporting Information), and the high number shown by (***P***)-**1** shows its importance in the CPL emitters. To the best of our knowledge, (***P***)-**1** exhibits one of the highest B_{CPL} reported to date among 7-helical bilayer nanographenes (Table S4, Supporting Information).

Time-dependent density functional theory (TD-DFT) calculations were conducted to better understand the link between the molecular structure and chiroptical properties of compounds **1-3**. The computational results indicate that the CD response exhibiting the highest g_{abs} is attributable to the $S_0 \rightarrow S_1$ electronic transition. **Figure** 6a–c presents the computed electric transition dipole moments (μ_e), magnetic transition dipole moments (μ_m), and the angle between them (θ). The calculation $g = 4 \cos\theta \times |\mu_m|/|\mu_e|$ indicates that the angle θ is essential in ascertaining the magnitude of the g-factor. These calculations indicate that compound (**1**) possesses the highest $|\mu_m|/|\mu_e|$ ratio and the lowest θ value, yielding the largest computed g-factor among the three compounds. The computed prediction aligns well with the experimental findings. Conversely, the θ values incrementally rise from compound (**1**) to compound (**2**) to compound (**3**), resulting in a systematic reduction in $\cos\theta$ and, therefore, diminished g-factors (Figure 6a–c). The computed dissymmetry factors for compounds **1**, **2**, and **3** are 7.3×10^{-3}, 5.6×10^{-4}, and 3.5×10^{-3}, respectively, demonstrating strong concordance with experimental values, except for **2**. The AICD plot[53] (Figure S28, Supporting Information) offers substantial support for the aromatic nature of all compounds **1-3**. A robust, persistent diatropic (counter-clockwise) ring current, represented by green vector arrows, is identified as delocalized throughout each layer of nanographene. The continuous current flow validates the local aromaticity of the individual rings and the global aromaticity of the extensive π-conjugated helicene bilayer nanographene.[54]

3. Conclusion

In summary, we have developed a versatile and modular synthetic approach to a new class of *bay*-functionalized [7]helicene bilayer nanographenes. By strategically incorporating methoxy, diketone, and methoxyphenazine substituents, we demonstrated precise control over their structural, photophysical, electrochemical, and chiroptical properties. Our detailed investigations, including single-crystal X-ray diffraction, revealed how these functional groups influence interlayer interactions and molecular geometry. Notably, optical studies showed a significant red shift in emission and enhanced fluorescence quantum yields (up to 55%), alongside extended fluorescence lifetimes (up to 10 ns) for the methoxyphenazine derivative. Electrochemical analysis highlighted a tunable HOMO–LUMO gap, while chiroptical measurements confirmed robust electronic circular dichroism and exceptional circularly polarized luminescence activity, with CPL brightness values reaching an impressive 110 M^{-1} cm^{-1}. These findings collectively establish *bay*-functionalized [7]HBNGs as a highly promising and tunable platform for the rational design of next-generation optoelectronic and chiral photonic materials. Looking ahead, we recognize the need for more scalable and device-oriented chiral materials. In this context, future work will focus on developing enantioselective synthetic strategies to access single-handed [7]HBNGs without chiral resolution on HPLC.

Supporting Information

Supporting Information is available from the Wiley Online Library or from the author.

Acknowledgements

A.K. acknowledges EPSRC New Horizon Award EP/V048112/1, EPSRC Strategic Equipment Grant EP/W006502/1 and EPSRC Germany-UK Collaborative Research Seed Funding in Semiconductor Security UKRI3223. This work was partially supported by a Royal Society grant ICA\R1\231014. A.K. acknowledges a Presidential Fellowship from the University of Manchester. A.K. and A.T. acknowledge EPSRC DTG studentship (EP/T517823/1, studentship 2657922). L.M. would like to thank the EPSRC and SFI Centre for Doctoral Training in Advanced Characterisation of Materials (Grant Ref: EP/S023259/1) and Diamond Light Source Ltd. for funding a PhD studentship. J.W. thanks the Royal Society (URF\R1\231732). The authors would like to thank Diamond Light Source for beamtime (proposal cy31541) and the staff of beamline I19 for their assistance. The authors acknowledge the support from NMR and the Mass Spectrometry and Separations Facility in the Department of Chemistry at the University of Manchester. A.T. thanks Mr. Joseph Moores, Phenomenex, for training and help with HPLC chiral column screening.

Open access publishing facilitated by Consiglio Nazionale delle Ricerche, as part of the Wiley - CRUI-CARE agreement.

Conflict of Interest

The authors declare no conflicts of interest.

Data Availability Statement

The data that support the findings of this study are available in the supplementary material of this article.

Keywords

bay-functionalization, bilayer nanographene, circular dichroism, circularly polarized luminescence, helicenes

Received: November 21, 2025
Revised: January 1, 2026
Published online:

---

[1] P. Izquierdo-Garcia, J. M. Fernandez-Garcia, N. Martín, *J. Am. Chem. Soc.* **2024**, *146*, 32222.
[2] K. A. Ritter, J. W. Lyding, *Nat. Mater.* **2009**, *8*, 235.
[3] S.-Y. Li, L. He, *Front. Phys.* **2022**, *17*, 33201.
[4] Y. Fogel, M. Kastler, Z. Wang, D. Andrienko, G. J. Bodwell, K. Mullen, *J. Am. Chem. Soc.* **2007**, *129*, 11743.
[5] R. K. Dubey, M. Melle-Franco, A. Mateo-Alonso, *J. Am. Chem. Soc.* **2021**, *143*, 6593.
[6] S. M. Draper, D. J. Gregg, R. Madathil, *J. Am. Chem. Soc.* **2002**, *124*, 3486.
[7] M. Stepien, E. Gonka, M. Zyla, N. Sprutta, *Chem. Rev.* **2017**, *117*, 3479.
[8] Y. Shen, C. F. Chen, *Chem. Rev.* **2012**, *112*, 1463.
[9] Y. J. Shen, N. T. Yao, L. N. Diao, Y. Yang, X. L. Chen, H. Y. Gong, *Angew. Chem. Int. Ed.* **2023**, *62*, 202300840.
[10] C. M. Cruz, S. Castro-Fernández, E. Maçôas, J. M. Cuerva, A. G. Campaña, *Angew. Chem. Int. Ed.* **2018**, *57*, 14782.
[11] V. Kumar, J. L. Páez, S. Míguez-Lago, J. M. Cuerva, C. M. Cruz, A. G. Campaña, *Chem. Soc. Rev.* **2025**, *54*, 4922.
[12] P. J. Evans, J. Ouyang, L. Favereau, J. Crassous, I. Fernández, J. Perles, N. Martín, *Angew. Chem. Int. Ed.* **2018**, *57*, 6774.
[13] G. Wang, M. Yu, X. Feng, *Chem. Soc. Rev.* **2021**, *50*, 2388.
[14] A. Chiesa, A. Privitera, E. Macaluso, M. Mannini, R. Bittl, R. Naaman, M. R. Wasielewski, R. Sessoli, S. Carretta, *Adv. Mater.* **2023**, *35*, 2300472.
[15] B. P. Bloom, Y. Paltiel, R. Naaman, D. H. Waldeck, *Chem. Rev.* **2024**, *124*, 1950.
[16] J. Tucek, P. Blonski, J. Ugolotti, A. K. Swain, T. Enoki, R. Zboril, *Chem. Soc. Rev.* **2018**, *47*, 3899.
[17] M. G. Rong, J. Wang, J. Liu, , *Chem Asian J.* **2021**, *16*, 1216.
[18] Y. Zhu, J. Wang, *Acc. Chem. Res.* **2023**, *56*, 363.
[19] M. A. Majewski, M. Stepien, *Angew. Chem. Int. Ed.* **2019**, *58*, 86.
[20] Y. Zhang, S. H. Pun, Q. Miao, *Chem. Rev.* **2022**, *122*, 14554.
[21] M. Cei, L. Di Bari, F. Zinna, *Chirality* **2023**, *35*, 192.
[22] P. Izquierdo-García, J. M. Fernández-García, S. Medina Rivero, M. Šámal, J. Rybáček, L. Bednárová, S. Ramírez-Barroso, F. J. Ramírez, R. Rodríguez, J. Perles, D. García-Fresnadillo, J. Crassous, J. Casado, I. G. Stará, N. Martín, *J. Am. Chem. Soc.* **2023**, *145*, 11599.
[23] S. D. Dongre, G. Venugopal, V. Kumar, A. Badrinarayan Jadhav, J. Kumar, S. Santhosh Babu, *Angew. Chem. Int. Ed.* **2024**, *64*, 202420767.
[24] M. S. H. Salem, R. Sharma, S. Suzuki, Y. Imai, M. Arisawa, S. Takizawa, *Chirality* **2024**, *36*, 23673.
[25] F. Morita, Y. Kishida, Y. Sato, H. Sugiyama, M. Abekura, J. Nogami, N. Toriumi, Y. Nagashima, T. Kinoshita, G. Fukuhara, M. Uchiyama, H. Uekusa, K. Tanaka, *Nat. Synth.* **2024**, *3*, 774.
[26] Y. Chen, C. Lin, Z. Luo, Z. Yin, H. Shi, Y. Zhu, J. Wang, *Angew. Chem. Int. Ed.* **2021**, *60*, 7796.
[27] W. Niu, Y. Fu, Q. Deng, Z. L. Qiu, F. Liu, A. A. Popov, H. Komber, J. Ma, X. Feng, *Angew. Chem. Int. Ed.* **2024**, *63*, 202319874.
[28] J. Lión-Villar, J. M. Fernández-García, S. Medina Rivero, J. Perles, S. Wu, D. Aranda, J. Wu, S. Seki, J. Casado, N. Martín, *Nat. Chem.* **2025**, *17*, 1099.
[29] G. F. Huo, W. T. Xu, J. Hu, Y. Han, W. Fan, W. Wang, Z. Sun, H. B. Yang, J. Wu, *Angew. Chem. Int. Ed.* **2025**, *64*, 202416707.
[30] V. Kumar, G. Venugopal, A. B. Jadhav, S. D. Dongre, R. Gonnade, J. Kumar, P. C. Ruer, B. Hupp, A. Steffen, S. S. Babu, *Angew. Chem. Int. Ed.* **2025**, *64*, 202422125.
[31] X. Y. Wang, X. Yao, A. Narita, K. Mullen, *Acc. Chem. Res.* **2019**, *52*, 2491.
[32] S. Qiu, A. C. Valdivia, W. Zhuang, F. F. Hung, C. M. Che, J. Casado, J. Liu, *J. Am. Chem. Soc.* **2024**, *146*, 16161.
[33] X. Y. Wang, J. Bai, Y. J. Shen, Z. A. Li, H. Y. Gong, *Angew. Chem. Int. Ed.* **2025**, *64*, 202417745.
[34] W. Niu, Y. Fu, Z. L. Qiu, C. J. Schurmann, S. Obermann, F. Liu, A. A. Popov, H. Komber, J. Ma, X. Feng, *J. Am. Chem. Soc.* **2023**, *145*, 26824.
[35] Y. Y. Ju, L. Chai, K. Li, J. F. Xing, X. H. Ma, Z. L. Qiu, X. J. Zhao, J. Zhu, Y. Z. Tan, *J. Am. Chem. Soc.* **2023**, *145*, 2815.
[36] L. Yang, Y. Y. Ju, M. A. Medel, Y. Fu, H. Komber, E. Dmitrieva, J. J. Zhang, S. Obermann, A. G. Campaña, J. Ma, X. Feng, *Angew. Chem. Int. Ed.* **2023**, *62*, 202216193.
[37] P. Izquierdo-Garcia, J. M. Fernandez-Garcia, J. Perles, N. Martín, *J. Am. Chem. Soc.* **2024**, *146*, 34943.
[38] M. Buendía, J. M. Fernández-García, J. Perles, S. Filippone, N. Martín, *Nat. Synth.* **2024**, *3*, 545.
[39] M. Kos, T. Beranek, I. Cisarova, P. Curinova, J. Zadny, J. Storch, V. Cirkva, M. Jakubec, *J. Org. Chem.* **2024**, *89*, 7495.
[40] J. A. Weber, E. L. Clennan, N. Arulsamy, *Eur. J. Org. Chem.* **2022**, *2022*, 202101533.
[41] Y. Yamamoto, H. Sakai, J. Yuasa, Y. Araki, T. Wada, T. Sakanoue, T. Takenobu, T. Kawai, T. Hasobe, *Chem. Eur. J.* **2016**, *22*, 4263.
[42] H. Sakai, S. Shinto, Y. Araki, T. Wada, T. Sakanoue, T. Takenobu, T. Hasobe, *Chem. - Eur. J.* **2014**, *20*, 10099.
[43] T. Qin, G. Zhou, H. Scheiber, R. E. Bauer, M. Baumgarten, C. E. Anson, E. J. List, K. Mullen, *Angew. Chem. Int. Ed.* **2008**, *47*, 8292.
[44] K. Li, Z. Sun, *Chem. Lett.* **2023**, *52*, 348.
[45] Y. Yuan, K.-C. Lo, L. Szeto, W.-K. Chan, *J. Org. Chem.* **2020**, *85*, 6372.
[46] C. Huang, M. Zheng, J. Xu, Y. Zhang, *Molecules* **2013**, *18*, 2942.
[47] M. Roy, V. Berezhnaia, M. Villa, N. Vanthuyne, M. Giorgi, J. V. Naubron, S. Poyer, V. Monnier, L. Charles, Y. Carissan, D. Hagebaum-Reignier, J. Rodriguez, M. Gingras, Y. Coquerel, *Angew. Chem. Int. Ed.* **2020**, *59*, 3264.
[48] Y. Nakakuki, T. Hirose, H. Sotome, H. Miyasaka, K. Matsuda, *J. Am. Chem. Soc.* **2018**, *140*, 4317.
[49] M. Jakubec, S. Hansen-Trooyen, I. Cisarova, J. Sykora, J. Storch, *Org. Lett.* **2020**, *22*, 3905.
[50] Y. J. Shen, N. T. Yao, L. N. Diao, Y. Yang, X. L. Chen, H. Y. Gong, *Angew. Chem. Int. Ed.* **2023**, *62*, 202300840.
[51] L. Arrico, L. Di Bari, F. Zinna, *Chem. Eur. J.* **2021**, *27*, 2920.
[52] Y. Nagata, T. Mori, *Frontiers in Chemistry* **2020**, *8*, 448.
[53] D. Geuenich, K. Hess, F. Köhler, R. Herges, *Chem. Rev.* **2005**, *105*, 3758.
[54] R. Herges, D. Geuenich, *J. Phys. Chem.* **2001**, *105*, 3214.